International Journal of Nanomedicine Dovepress

Open Access Full Text Article ORIGINAL RESEARCH

Mesoporous Polydopamine Nanotherapeutics for MRI-Guided Cancer Photothermal and Anti-Inflammatory Therapy

Yang Liu[1,*], Chunan Wang[1,*], Sitong Liu[1,*], Hangzhan - Ma[2], Jiayun Xu[3], Kai Jiang[1], Ruitao Lu[4], Xintao Shuai[5], Jinming Wang[3], Zhong Cao[1]

[1]School of Biomedical Engineering, Sun Yat-Sen University, Guangzhou, Guangdong, People's Republic of China; [2]Department of Orthopedics, Panyu Hospital of Chinese Medicine, Guangzhou, Guangdong, People's Republic of China; [3]Department of Oral Implantology, Guanghua School of Stomatology, Hospital of Stomatology, Sun Yat-sen University, Guangdong Provincial Key Laboratory of Stomatology, Guangzhou, People's Republic of China; [4]Shenzhen International Institute for Biomedical Research, Shenzhen, Guangdong, People's Republic of China; [5]Nanomedicine Research Center, The Third Affiliated Hospital of Sun Yat-Sen University, Guangzhou, Guangdong, People's Republic of China

*These authors contributed equally to this work

Correspondence: Zhong Cao; Jinming Wang, Email caozhong@mail.sysu.edu.cn; wjinm@mail.sysu.edu.cn

Background: As a burgeoning cancer treatment modality, photothermal therapy (PTT) has shown robust anti-tumor effects. However, it still faces numerous challenges, such as triggering an inflammatory response and potentially increasing the risk of cancer recurrence. To address these concerns, integration of PTT with anti-inflammatory therapies presents a promising approach to enhance the efficacy of cancer treatment and meanwhile reduce the risk of recurrence.

Methods: In this study, Gd^{3+} was first chelated with dopamine to create Gd-DA chelates, and then the mesoporous dopamine nanoparticles MX@Arg-Gd-MPDA (MAGM NPs) were synthesized by combining arginine (Arg) and the anti-inflammatory medication meloxicam (MX). The photothermal properties of MAGM NPs were then defined and examined; the in vivo MRI imaging effect, as well as MAGM NPs' anti-cancer and anti-inflammatory efficiency, were tested in a mouse model of breast cancer.

Results: The incorporation of Arg doping into MAGM NPs was intended to boost its photothermal conversion efficiency and reactive oxygen species (ROS) scavenging ability. Additionally, synergizing with the anti-inflammatory agent meloxicam (MX) within the nanoparticles aimed to enhance the anti-inflammatory effect following photothermal therapy. Furthermore, gadolinium ions (Gd^{3+}) were chelated into the nanostructure to enable precise T1-T2 dual-mode magnetic resonance imaging (MRI) of the intratumor accumulation profile. This imaging capability was leveraged to guide the implementation of photothermal therapy. Animal experiments demonstrated that MAGM NPs exerted a notable anticancer effect in a 4T1 breast cancer mouse model, under the precise guidance of MRI.

Keywords: magnetic resonance imaging, photothermal therapy, anti-inflammatory therapy, mesoporous polydopamine, cancer therapy

Introduction

Photothermal therapy (PTT) represents a promising cancer treatment technique that utilizes light and heat energy to selectively eliminate cancer cells. This approach has attracted significant attention and is currently undergoing extensive investigation for its therapeutic potential in cancer treatment. Recent advancements in photothermal conversion agents, such as gold nanoparticles,[1,2] graphene,[3,4] carbon nanotubes,[5,6] and mesoporous dopamine (MPDA),[7–9] have shown remarkable ability to absorb light energy upon exposure to near-infrared (NIR) light. PTT offers a promising approach for the effective and minimally invasive ablation of tumor tissue by significantly elevating the temperature at the tumor site. Despite showing promising anti-tumor effects in various studies, there are unavoidable challenges. For instance, upon inducing damage to tumor cells, PTT can prompt the release of intracellular components from the tumor into the extracellular environment, potentially instigating an inflammatory response thereafter. This cascade of responses typically involves the production of inflammatory factors, such as TNF-α, IL-1β, and IL-6,[10,11] which subsequently activate pro-survival genes within residual cancer cells,

Received: 11 March 2024
Accepted: 12 October 2024
Published: 25 October 2024

thereby increasing the risk of cancer recurrence. In response to these challenges, numerous researchers have embarked on pioneering studies combining PTT with anti-inflammatory strategies.[7,12–15] This approach aims to mitigate the inflammatory response associated with PTT, thereby enhancing its therapeutic efficacy and reducing the risk of cancer recurrence.

For effective PTT guidance, reduction of drug dosage, and mitigation of potential damage to normal tissues associated with thermotherapy, the utilization of appropriate medical imaging modalities is paramount. Among the array of imaging modalities available, magnetic resonance imaging (MRI) stands out as a well-established tool in clinical medicine owing to its non-invasive nature, excellent spatial resolution, soft-tissue contrast capability, and three-dimensional imaging proficiency.[16–18] In recent years, there has been widespread development of contrast agents (CAs) to enhance MRI imaging capabilities. However, commonly used T1 and T2 contrast agents come with inherent limitations.[19] T1 contrast agents have a short cycle time, and T2 contrast agents are prone to artifacts.[20–24] In response to these challenges, T1/T2 weighted bimodal imaging strategies for MRI have garnered considerable attention. T1/T2 bimodal imaging holds the promise of overcoming the aforementioned limitations, providing more accurate imaging information for improved PTT guidance and minimizing potential drawbacks associated with thermotherapy. For instance, Li et al demonstrated the self-assembly of gadolinium nanoparticles (DOTA-Gd-CBT NPs) through in situ π-π stacking, resulting in the formation of the Glu-DOTA-Gd-CBT NPs.[25] Noteworthy is the capability of these nanoparticles to enhance both T1 and T2 MRI imaging in a nude mouse model of hepatocellular carcinoma. Moreover, the encapsulation of various drugs within the contrast agent enables the visualization of drug delivery processes, enhancing cancer therapy by precisely delivering drugs to the cancer imaging site.[26] The integration of bimodal imaging agents and photothermal therapeutic agents into a nanoplatform allows for the accurate localization of tumor location, determination of tumor size, and monitoring of the biodistribution of the nanocomplexes following drug administration. This line of research holds great promise for MRI-guided precision cancer photothermal therapy.

Mesoporous dopamine (MPDA) nanoparticles have attracted attention due to their simple synthesis and biocompatibility. These nanoparticles, resembling melanin-like polymers, exhibit inherent properties such as its robust free radical scavenging ability and exceptional photothermal characteristics, have been demonstrated in numerous studies, showcasing its efficacy in promoting the ablation of tumor tissues under near-infrared light irradiation.[27,28] Recently, according to the discovery of Prof. Yiwen Li's team, doping arginine in the synthesis of mesoporous polydopamine nanoparticles can disrupt the dense microstructure of dopamine oligomers to form a weak polymer, which improves the photo-thermal conversion ability as well as scavenging of free radicals, and this discovery provides a new strategy for the development of MPDA materials.[29,30] Additionally, MPDA demonstrates remarkable metal-chelating capabilities, serving as ionic anchors for various metal ions, including Mn^{2+},[31,32] among others.[33,34] This property has been substantiated in diverse studies, highlighting MPDA's potential for MRI imaging. Importantly, MPDA's porous structure facilitates the adsorption of chemotherapeutic drugs like doxorubicin (DOX) and anti-inflammatory compounds such as meloxicam (MX) through π-π interactions.[35] This feature not only enables efficient drug delivery but also enhances the inhibition of cancer. Therefore, MPDA emerges as a promising candidate for anti-tumor photothermal therapy, offering the potential for precise imaging in cancer treatment.

Herein, we present a strategy to synthesize a mesoporous nanoparticles MX@Arg-Gd-MPDA denoted as MAGM NPs (Figure 1A). The incorporation of Arg into MAGM NPs is anticipated to yield a dual enhancement effect, augmenting both its free radical scavenging ability and photothermal conversion efficiency. Moreover, MAGM NPs demonstrates effectiveness in mitigating PTT-induced inflammation through the controlled release of the drug MX. Additionally, the Gd^{3+}-chelated form of MAGM NPs may provide precise T1-T2 dual-mode MRI guidance for PTT (Figure 1B). Consequently, this multifunctional NPs is poised to offer a comprehensive visualization strategy for the simultaneous implementation of photothermal and anti-inflammatory treatments in cancer therapy.

Experimental Section

Materials and Reagents

Dopamine hydrochloride (98%), L-Arginine (98%) and Meloxicam (98%) were purchased from Aladdin. 1,3,5-Trimethylbenzene (99%), Trimethylol aminomethane (99%) and Pluronic F-127 (BR) were acquired from Sigma-Aldrich, Gadolinium trichloride hexahydrate ($GdCl_3.6H_2O$) (99%) were obtained from Shanghai Rhawn Chemical Technology Co., Ltd., other reagents were purchased from Sui hui Biology (Guangzhou, China) and used without further

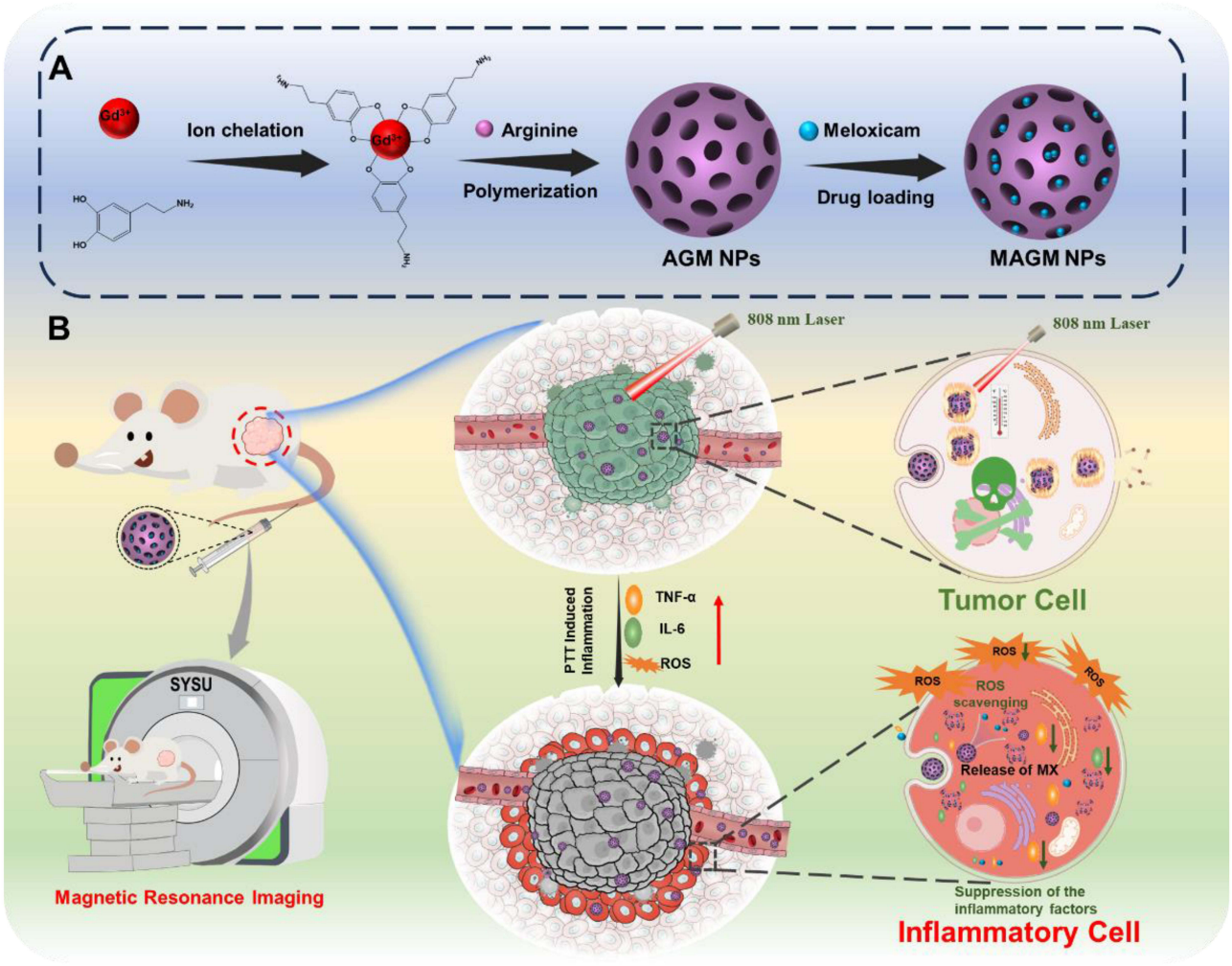

Figure 1 A schematic diagram of MAGM preparation (**A**) and MAGM for MRI-guided photothermal/anti-inflammatory treatment of tumors (**B**).

purification. In addition, 4T1 cell line and RAW264.7 cell line were purchased from the Animal Experiment Center of Sun Yat-sen University.

Mouse breast cancer cells (4T1) and Mouse-derived macrophages (RAW264.7) were cultured in high glucose medium (DMEM) containing 10% fetal bovine serum (FBS), 100 μg/mL penicillin and 100 μg/mL streptomycin. The culture conditions were 37°C and 5% CO_2.

Preparation and Characterization of MAGM NPs

Synthesis of Arg-Gd-MPDA (AGM)

AGM synthesized according to the following steps. Initially, 90 mg of dopamine hydrochloride and 4 mg of gadolinium chloride hexahydrate were dissolved in ultrapure water and stirred for 24 hours under dark conditions to obtain a dopamine-gadolinium chelating solution. Subsequently, 36 mg of F-127 was weighed and mixed with ultrapure water (6 mL), anhydrous ethanol (6 mL), and the dopamine-gadolinium (Gd-DA) chelating solution (300 μL). The mixture was then stirred in the dark for 20 minutes to ensure thorough mixing. Additionally, 300 μL of TMB emulsion was added dropwise and the mixture was ultrasonically shaken for 4 minutes until it turned milky white. Subsequently, 1 mL of arginine solution (18 mg/mL) was slowly added under magnetic stirring and the reaction proceeded for 8 hours in darkness. The resulting AGM were collected by centrifugation at 13000 rpm for 10 minutes and washed with ethanol and ultrapure water. Gd-MPDA (GM) was prepared using the same method, with tris buffer (20 mg/mL) replacing the arginine solution, for subsequent experiments.

Preparation of MAGM NPs

The UV-vis absorption spectra of meloxicam (MX) were obtained using a UV-vis spectrometer (DU730, US). The standard curve of MX in a mixed solvent of DMSO and water with a volume ratio of 3:1 was fitted based on the absorbance at the maximum absorption wavelength (270 nm). The AGM sample (1 mg/mL) was mixed with different concentrations of MX solution (0.5, 1, 1.5, 2 mg/mL) and stirred for 24 hours to collect MAGM NPs. All the supernatant was collected to measure absorbance at 270 nm. The MX content in the supernatant was calculated based on the standard curve of MX. The drug loading capacity (LC) and encapsulation efficiency (EE) were calculated using Formulas (1) and (2) to determine the optimal feed ratio.

$$\text{Drug loading capacity (DLC) \%} = \frac{m_2 - m_1}{m_0 + (m_2 - m_1)} \times 100\% \quad (1)$$

$$\text{Encapsulation efficiency (EE) \%} = \frac{m_2 - m_1}{m_2} \times 100\% \quad (2)$$

Where m_0 is the mass of AGM, m_1 is the mass of MX in supernatant, m_2 is the total input of MX.

Characterization of Nanoparticles

The MX, AGM, and MAGM NPs were diluted and ultrasonically dispersed. The size and zeta potential of the nanoparticles were measured using a Malvern Mastersizer particle sizer (Zetasizer Nano ZS90, UK). Additionally, the size and morphology of the nanoparticles were studied by transmission electron microscopy (TEM) using a FEI Tecnai G2 F30 microscope (Holland) operating at 200 kV. After drying the AGM powder using a freeze dryer, N_2 desorption experiments were conducted using a specific surface area and pore space analyzer (NOVA, US). The specific surface area and pore size distribution of AGM were then calculated using the BET and BJH methods, respectively. The UV-visible absorption spectra (UV-Vis) were obtained by taking 2 mL of GM, AGM and MAGM NPs and scanning them at 190–1100 nm wavelengths under a UV spectrophotometer (DU730, USA). To assess the stability of MAGM NPs, the nanoparticles were evaluated in various buffer solutions, including deionized water, PBS, and DMEM. Their physico-chemical properties, such as size and zeta potential, were measured at multiple time points. Finally, the elemental composition of MAGM NPs was explored., including carbon (C), oxygen (O), nitrogen (N), and gadolinium (Gd) in MAGM NPs, was analyzed using energy-dispersive X-ray spectroscopy (EDS) in the TEM. The content of Gd in AGM nanoparticles was determined by inductively coupled plasma atomic emission spectroscopy (ICP-AES) (IRIS (HR), TJA Corporation, US). The nitrogen(N) content of AGM was determined using an elemental analyzer. Subsequently, the arginine (Arg) content in AGM was calculated using Formula (3).

$$N_{\text{GM}} \times (1 - x) + N_{\text{A}} \times x = N_{\text{AGM}} \quad (3)$$

where N_{GM} is the N content in GM, N_A is the N content in arginine (32.18%, wt %), N_{AGM} is the N content in AGM.

In vitro Drug Release Studies

1 mg/mL solution of MAGM NPs (or an equivalent amount of MX solution) was placed into a 3500 Da dialysis bag, sealed, and then immersed in a centrifuge tube as previously described. The tubes were incubated in a shaker at 37°C (100 rpm) in the dark. At various time points, 2 mL of buffer was removed and replaced with 2 mL of fresh buffer to continue the experiment. The absorbance of the buffer at 360 nm was measured using a UV spectrophotometer, and the cumulative release rate of MX was calculated using the standard curve of MX in the buffer and Equation (4).

$$\text{Cumulative drug release rate (\%)} = \frac{c_n \times V_0 + \sum c_{n-1} \times V_1}{m_0} \times 100\% \quad (4)$$

Where c_n or c_{n-1} denotes the concentration of MX in the buffer taken out at the n or n-1 time, V_0 denotes the total volume of the buffer (20 mL), V_1 denotes the volume of the sample taken out each time (2 mL), and m_0 denotes the total amount of drug in the sample.

In vitro Photothermal Properties

The photothermal conversion efficiency and photothermal stability of MAGM NPs were investigated. For photothermal conversion efficiency assessment, 2 mL of MAGM NPs solution (100 μg/mL) was irradiated with 808 nm NIR (1 W/cm^2) until it reached a stable temperature, after which it was allowed to cool naturally. The real-time temperature during the entire heating and cooling process was recorded, and the photothermal conversion efficiency of MAGM NPs was calculated. Subsequently, the photothermal stability of MAGM NPs (100 μg/mL) was evaluated by subjecting it to four cycles of NIR irradiation (1 W/cm^2 for 15 minutes per cycle).

Free Radical Scavenging Performance

We confirmed the free radical scavenging ability of the materials using the DPPH assay and the salicylic acid (SA) method. The scavenging rates of DPPH and ·OH radicals were calculated according to Formula (5).

$$\text{Clearance rate}\,(\%)=\frac{A_0-A_x}{A_0}\times 100\% \tag{5}$$

where *A0* represents the initial absorbance, and *Ax* represents the absorbance at different times.

In vitro MRI

In vitro magnetic resonance imaging (MRI) was conducted using both a 3 Tesla (3 T) MRI scanner and a 7 Tesla (7 T) MRI scanner. The relaxation rate, often denoted as r1 or r2, is a critical parameter in magnetic resonance imaging (MRI) that reflects the speed at which nuclear magnetization returns to equilibrium after excitation. Typically, r_1 is associated with longitudinal relaxation (T1 relaxation), while r_2 pertains to transverse relaxation (T2 relaxation). In MRI experiments, the relaxation rates r_1 and r_2 can be determined by plotting the reciprocal of the relaxation time (1/T1 or 1/T2) against the concentration of the contrast agent.

Gd-DTPA, AGM, and MAGM NPs samples were prepared at different concentrations, and then subjected to T1 and T2 weighted imaging using a 3 T MRI scanner (Ingenia DNA2, Philips, Holland). For r_1 measurement, the reciprocal of the T1 relaxation time (1/T1) is plotted against the concentration of the contrast agent (Gd concentration in mM). The slope of the linear fit of this plot provides the r1 relaxation rate, which is expressed in units of s^{-1} (seconds to the power of minus one). T1-weighted MRI parameters: TR = 500 ms, TE = 15 ms, slice thickness = 1 mm; Similarly, for r_2 measurement, the reciprocal of the T2 relaxation time (1/T2) is plotted against the concentration of the contrast agent. The slope of the linear fit of this plot yields the r_2 relaxation rate, also in units of s^{-1}. T2-weighted MRI parameters: TR = 2000 ms, TE = 100 ms, slice thickness = 1 mm.

Gd-DTPA, AGM, and MAGM were diluted across a gradient of concentrations. Subsequently, equal proportions of the diluted sample solution and a 4% gelatin solution (wt %) were mixed thoroughly. Following proper mixing, the samples underwent T1 and T2 weighted imaging using a 7 Tesla (7 T) MRI scanner (PharmaScan70/16, Bruker, Germany). T1-weighted MRI parameters: TR = 867 ms, TE = 6.92 ms, slice thickness = 1 mm; T2-weighted MRI parameters: TR = 3000 ms, TE = 10 ms.

Evaluation of Anti-Tumor Effects in vitro

Cytotoxicity assays were conducted using the CCK-8 kit (Beyotime, China) following the manufacturer's protocol. Initially, 4T1 cells were seeded in 96-well plates at a density of 5×10^3 cells/well and incubated for 24 hours to allow cell adhesion. Subsequently, the cells were treated with varying concentrations of MX, AGM, or MAGM NPs. After a 6-hour incubation period, the AGM and MAGM groups were subjected to NIR irradiation (808 nm, 1 W/cm^2, 3 min). Following 24 hours of further incubation, CCK-8 solution was added to each well. After an additional 3-hour incubation, the microplate reader was utilized to measure the absorbance at 450 nm, and the cell viability was subsequently determined through the application of a specific Formula (6).

$$\text{Cell viability}\,(\%)\ =\frac{A_x-A_2}{A_1-A_0}\times 100\% \tag{6}$$

where A_0 represents the absorbance value of the medium containing CCK8, A_1 represents the absorbance value of the medium, cells, and CCK8, A_2 represents the absorbance value of the medium containing CCK8 and the sample, and A_x represents the absorbance value of the medium, cells, CCK8, and the sample. Prior to conducting internalization/uptake studies in cells, these values were confirmed using fluorescence spectra and fluorescence microscopy.

Cellular uptake of samples was monitored using flow cytometry detection (FACS Calibur, BD, US) and confocal imaging microscopy (FV3000, OLYMPUS, Japan). In brief, 6-coumarin dye-labeled AGM (C6@AGM) were incubated with 4T1 cells for different time points. Subsequently, the cells were centrifuged to collect and then resuspended in PBS buffer. The cell suspension was then analyzed by flow cytometry. To further validate the results, the nuclei were stained with DAPI (4′,6-diamidino-2-phenylindole, Life Technologies) for 10 minutes. After staining, the DAPI dye was removed, and the cells were washed with PBS. The samples were then collected and observed for fluorescence signals using confocal laser scanning microscopy (CLSM). Next, live/dead staining was conducted using the Calcein-AM/PI Double Stain Kit (Beyotime, China), and representative images were captured with a fluorescence microscope (IX70, OLYMPUS, Germany). The numbers of live and dead cells were counted using Image J software. Additionally, the Annexin V-FITC/PI kit was employed to study the apoptosis and necrosis of 4T1 cells treated with different samples.

Anti-Inflammatory Effect of MAGM NPs in vitro

The cytotoxicity and cell uptake studies of RAW 264.7 cells followed the same procedure as described above. Intracellular ROS levels were assessed using the ROS-sensitive DCFH-DA probe (Beyotime, China) as follows: RAW 264.7 cells were restimulated with lipopolysaccharide (LPS; 1 μg/mL). ROS inhibition was achieved by treating RAW 264.7 cells with MX, AGM, or MAGM NPs solutions (80 μg/mL) in 6-well plates for 24 h. Subsequently, 1 mL of DCFH-DA solution (10 μM) was added to each well and incubated for 30 min. After washing and collecting the cells into a flow tube, intracellular fluorescence intensity was measured using flow cytometry. For CLSM observation, the cells were fixed with 4% paraformaldehyde at 4°C for 10 min after staining with DCFH-DA. Subsequently, the cells were washed twice with PBS, and DAPI dye was added to incubate for another 10 minutes. Finally, the fluorescence signal was observed using CLSM.

Cellular cytokine detection was primarily performed using specific ELISA assay kits. Initially, 4T1 cells and RAW264.7 macrophages were separately seeded in a 6-well culture plate and incubated in a suitable medium for 24 hours to achieve the desired cell density. Subsequently, the original culture medium was replaced with a medium containing 80 μg/mL (concentration of AGM) of MX, AGM, or MAGM NPs, while a blank group was established with an equivalent amount of PBS as a control. The cells were then co-cultured in the new medium (6 h). For the light exposure group, the cells were irradiated with an 808 nm near-infrared laser for 5 minutes at a power density of 1 W/cm² to observe the effect of light on cytokine production. After co-culturing (4 h), the supernatant from each well of the 4T1 cells was transferred to a separate 6-well plate containing RAW264.7 macrophages for further cultivation. As a positive control, one well of RAW264.7 macrophages was cultured with a medium containing lipopolysaccharide (LPS) at a concentration of 1 μg/mL to induce an inflammatory response. After co-culturing for 24 hours, the supernatant from each well was collected, and the levels of pro-inflammatory cytokines (IL-6, TNF-α) were measured using ELISA assay kits (Elabscience, China) to evaluate the regulatory effect of the nanomaterials on cytokine production.

In vivo Animal Studies

Male BALB/c mice were employed in this study to investigate the therapeutic effects of MX, AGM, and MAGM NPs on tumors. All animal experiments were conducted in compliance with the guidelines outlined in the "Animal Management Regulations' of the Ministry of Health of the People"s Republic of China and were approved by the Animal Care and Use Committee of Sun Yat-sen University. Female BALB/c mice aged 3 to 5 weeks were inoculated with 4T1 tumor cells (1×10^7/mL) on the right back to establish a xenograft model for subsequent in vivo treatment.

Biodistribution of MAGM NPs in vivo

To assess the biodistribution of MAGM NPs in mice, fluorescently labeled MAGM NPs (Cy5.5@MAGM) was administered via tail vein injection into 4T1 tumor-bearing mice. At predefined time points, the in vivo fluorescence

distribution was captured using the IVIS Spectrum small animal imaging system (PerkinElmer IVIS Lumina III, US). At the conclusion of the experiment, one mouse from each group was randomly euthanized, and the major organs (heart, liver, spleen, lung, kidney) and tumor tissues were dissected and collected for fluorescence imaging analysis.

MR Imaging in vivo

To investigate the MRI effect of MAGM NPs in mice, three female BALB/c mice were injected with a specified amount of MAGM MPs solution via the tail vein. T1 and T2 weighted MRI scans of the tumor site in the mice were acquired using a 3T MRI scanner at various time points. The MRI parameters used were as follows: repetition time (TR) = 1600 ms, echo time (TE) = 65 ms, and slice thickness = 1 mm.

Antitumor Effect in vivo

BALB/c mice were employed to investigate the photothermal effects of MX, AGM, and MAGM NPs on tumors. Once the tumor volume reached approximately 100 mm^3 within one week, the mice were randomly assigned to six groups (n=5) as follows: (1) PBS; (2) MX; (3) AGM; (4) AGM+L; (5) MAGM; (6) MAGM+L. MX was administered once every 2 days for a total of 3 times. For the light group, the tumor site underwent irradiation with an 808 nm NIR laser (1 W/cm^2, 5 min) after 8 hours of administration. The therapeutic efficacy was assessed by monitoring the changes in relative tumor volume in mice. On the 20th day, the mice were euthanized, and the tumors were excised for tissue sectioning (4 mm thickness). Subsequently, the sections were subjected to H&E and TUNEL staining for analysis.

Anti-Inflammatory Effect in vivo

The 4T1 tumor-bearing mouse model was established using the method described above. After 3 days of administration, tumor tissues from each group of mice were collected. PBS with pH 7.4 was then added for tissue homogenization. The mixture was centrifuged at 3000 rpm for 20 minutes, and the resulting supernatant was collected for measurement using TNF-α and IL-6 ELISA kits.

In vivo Biosafety

In vivo biosafety assessment was conducted by monitoring the body weight of the mice every two days throughout the treatment period. Blood samples were collected from different groups at both the early and late stages of treatment for blood biochemical and blood routine tests. After completion of the treatment, tumor tissues from mice in each group were fixed with paraformaldehyde to prepare paraffin sections (4 mm thickness). Hematoxylin-eosin (HE) staining was performed on sections of the heart, liver, spleen, lung, and kidney for histological analysis, aimed at assessing the in vivo biosafety of MAGM NPs.

Results and Discussion

Preparation and Characterization of MAGM NPs

AGM was synthesized by polymerizing Gd-DA on a template formed by 1,3,5-trimethylbenzene and the block copolymer F127. This synthesis process occurred in an alkaline environment facilitated by arginine. Subsequently, the anti-inflammatory drug meloxicam (MX) was loaded into AGM through π–π interactions, resulting in the formation of MAGM NPs, which enhances the anti-inflammatory effects. To optimize the particle size, we adjusted the concentration ratios of DA to $GdCl_3 \cdot 6H_2O$, aiming to obtain mesoporous polydopamine with the most suitable size. The particle sizes of the nanoparticles produced from these varying ratios were determined using DLS, with the results provided in Table S1. According to DLS measurements (Figure S1), the average sizes of AGM and MAGM NPs were 223.5 nm and 227.4 nm, respectively, slightly larger than Gd-MPDA (213.4 nm). Moreover, zeta potential measurements of GM, AGM, and MAGM MPs indicated that the incorporation of arginine and the drug MX had minimal effect on the zeta potentials during the preparation process (Table S2). Subsequently, transmission electron microscopy (TEM) was conducted to observe the morphology (Figure 2A–C). GM, AGM, and MAGM MPs all exhibited similar spherical porous structures with sizes around 200 nm. These results suggest that the incorporation of arginine and subsequent loading of MX did not significantly affect the

morphology or particle size. N_2 desorption experiments were conducted to further characterize the mesoporous structure of AGM nanoparticles. As shown in Figure S2, the N_2 desorption curve of AGM exhibits a typical H3 hysteresis loop, confirming the presence of a mesoporous structure in AGM. Based on this, the specific surface area and pore size distribution of AGM were analyzed using the BET and BJH methods, respectively. The results indicate that AGM possesses a significantly higher specific surface area of approximately 50 m^2/g, compared to the previously reported polydopamine nanoparticles (9.2–19.9 m^2/g), with an average pore size of about 19 nm, which is favorable for drug loading.[36] The UV-visible absorption spectra of GM, AGM and MAGM NPs in aqueous solution were scanned by UV-visible spectrophotometer (Figure S3). The higher absorbance of AGM than GM at the same concentration was attributed to the fact that arginine doped inside of AGM constructed a donor-acceptor microstructure, which reduced the energy band gap and promoted electron transfer to enhance the light absorption. Compared with AGM, MAGM NPs has an obvious absorption peak at 360 nm, which proves the successful loading of MX. As illustrated in the energy dispersive spectrometer (EDS) analysis (Figure 2D), the four elements, C, N, O, and Gd, were uniformly distributed within AGM, with a Gd content of 3.06% (wt%) as determined by inductively coupled plasma atomic emission spectroscopy (ICP-AES). The chelation of Gd within AGM renders it suitable for use as an MRI contrast agent. Furthermore, the arginine doping content in AGM was calculated to be 3.22% based on the N element content. The porous structure of AGM significantly contributes to its high MX loading efficiency (36.1%). Additionally, the hydrophobic and π–π interactions between AGM and MX facilitate the controlled release of MX, making AGM a promising candidate for drug delivery applications. The release and diffusion of both loaded and free MX were studied under simulated physiological conditions in vitro. In addition, as shown in the results of Figure S4, the particle size and potential of MAGM NPs remained essentially unchanged during 14 days of preservation in different media, indicating that MAGM NPs can be stably preserved in different physiological environments for subsequent antitumor studies.

As depicted in Figure S5, approximately 65.7% of the free MX diffused into the buffer, with the release rate stabilizing at around 12 hours. In contrast, the release rate of MX from MAGM NPs was lower, reaching only 40.6% during the same period. However, MX continued to gradually diffuse from MAGM NPs into the buffer, resulting in a steadily increasing cumulative release rate over time. Furthermore, as shown in Figure S6, the temperature changes induced by transient photothermal conditions did not impact drug release from MAGM NPs. This observation suggests that MAGM NPs could serve as an effective MX delivery and sustained-release system for cancer therapy. Additionally, the temperature changes of GM, AGM, and MAGM NPs under 808 nm laser irradiation are recorded in Figure 2E, F and Figure S7. MAGM NPs and AGM exhibited a temperature increase of 34°C in 10 minutes, higher than that of GM by 22°C, demonstrating enhanced photothermal conversion ability due to the presence of Arg. Moreover, the temperature of MAGM NPs increased with both concentration and laser power, achieving a photothermal conversion efficiency of 56.5% and exhibiting excellent photothermal stability, as illustrated in Figure 2G and H. This may be attributed to the disruptive effect of Arg on the dense microstructure of polydopamine, which facilitates the formation of donor-acceptor structures within AGM. This structural modification promotes efficient electron transfer and reduces athermal radiative transitions, thus enhancing photothermal conversion.[29,30]

The DPPH and ˙OH radical scavenging properties of GM, AGM and MAGM NPs were assessed as shown in Figure 3A and B. DPPH scavenging experiments revealed that all three groups exhibited free radical scavenging ability (Figure 3A). Specifically, the GM group exhibited a DPPH scavenging rate of 41.7%, while the AGM and MAGM groups showed higher rates of 51.7% and 51.2%, respectively. This enhancement can be attributed to Arg disrupting the dense microstructure within polydopamine, leading to the formation of a weak polymer with stronger free radical trapping ability. Similar results were observed in ˙OH scavenging experiments (Figure 3B). Compared to the blank control group, solutions treated with GM, AGM, and MAGM NPs exhibited reduced ˙OH concentrations. The GM group exhibited a ˙OH scavenging rate of 19.3%, while the AGM and MAGM groups demonstrated similar rates of 60.7% and 58.9%, respectively, approximately three times higher than that of the GM group. This superior free radical scavenging ability is essential for alleviating inflammatory oxidative stress.

The MRI contrast capability of AGM was evaluated at both 3 T and 7 T field strengths and compared with Gd-DTPA, a clinically used contrast agent. Relaxation rates (r_1 and r_2) are crucial parameters in MRI as they directly affect image contrast and signal intensity, thereby influencing the diagnostic utility of MRI scans. MRI T1 signal intensity at 3 T of AGM exhibited

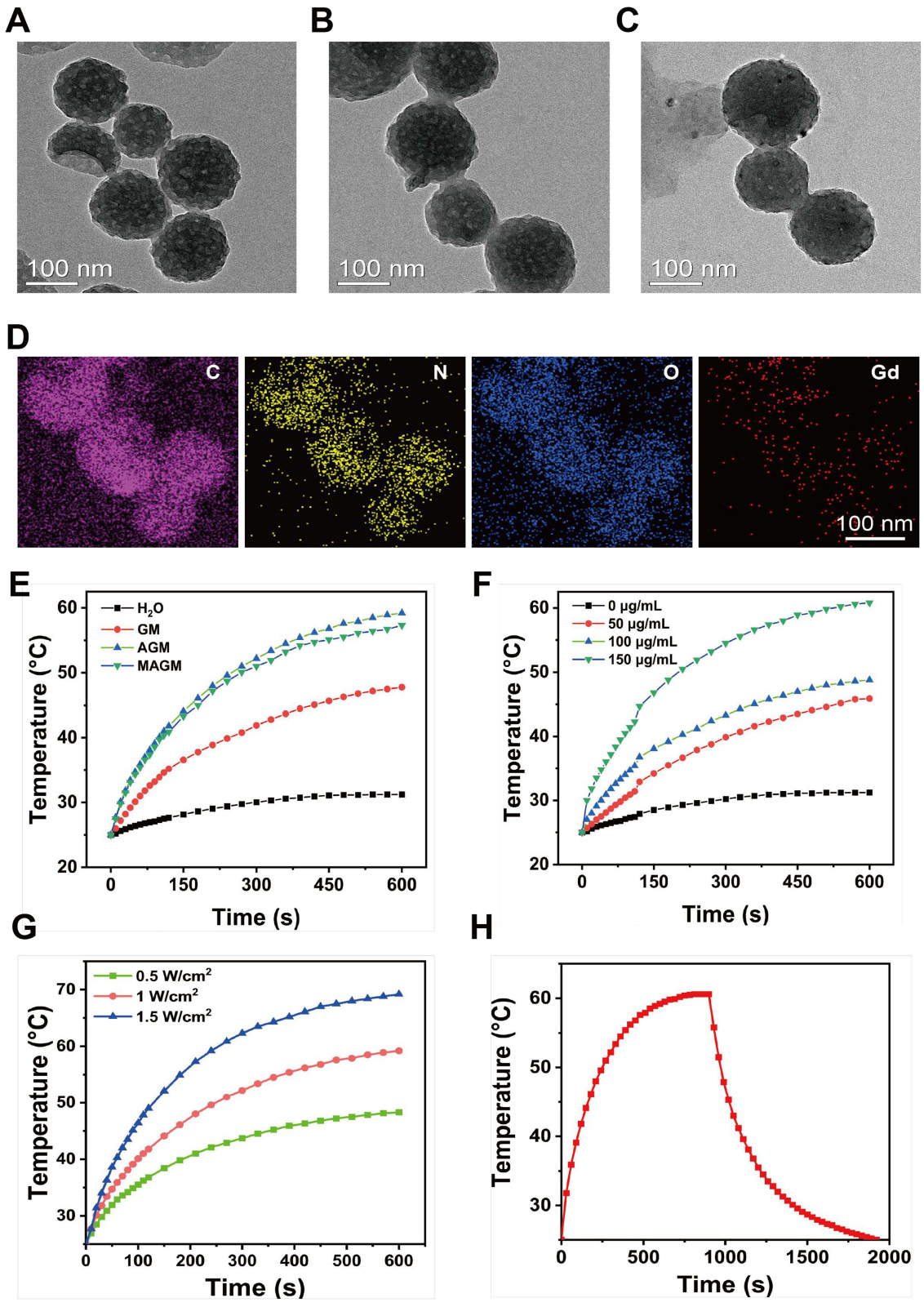

Figure 2 TEM images of (**A**) GM, (**B**) AGM and (**C**) MAGM; (**D**) EDS spectrum analysis of AGM. (**E**) Temperature changes of different sample; Temperature changes of MAGM under (**F**) different concentrations and (**G**) different irradiation power; (**H**) The photothermal conversion efficiency of MAGM (808 nm, 1 W/cm^2, 100 μg/mL).

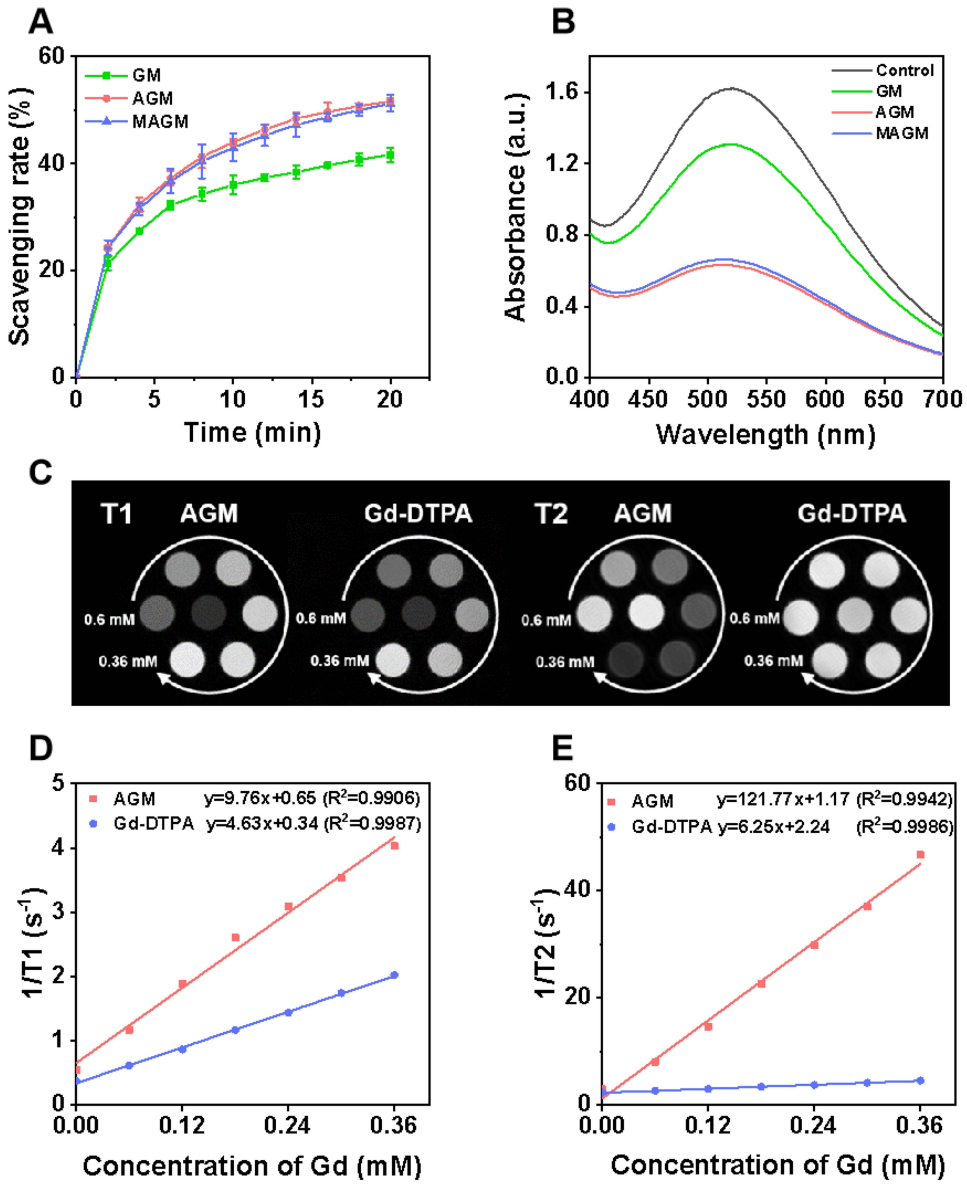

Figure 3 (**A**) DPPH scavenging rate of GM, AGM and MAGM (20 μg/mL) in 20 minutes. (**B**) UV-Vis absorption spectra of the solution treated with GM, AGM and MAGM (100 μg/mL). (**C**) T1-weighted and T2-weighted MRI of AGM and Gd-DTPA. (**D**) Longitudinal relaxation rates and (**E**) transverse relaxation rates of AGM and Gd-DTPA (Field strength=7 T).

superior contrast capability (Figure S8), displaying a much higher r_1 value (74.86 mM^{-1} s^{-1}) compared to Gd-DTPA (4.99 mM^{-1} s^{-1}). This enhancement in contrast capability may be attributed to the spatial structure of Gd-chelated mesoporous nanoparticles, which more significantly affect water molecule relaxation. Furthermore, AGM demonstrated a high r_2 value (70.66 mM^{-1} s^{-1}), a characteristic not typically observed with traditional Gd-based contrast agents.

In comparison, at a 7 T field strength (Figure 3C–E), the r_1 value of AGM decreased to 9.76 mM^{-1} s^{-1}, yet it remained higher than that of Gd-DTPA (4.63 mM^{-1} s^{-1}). This decrease in r_1 value for AGM could be attributed to changes in the interaction between AGM and water molecules with the increase in field strength, limiting the longitudinal relaxation process of water molecules. Conversely, Gd-DTPA, being a small molecule, was less affected by the field strength, and thus, no significant decline in relaxation rate occurred. Additionally, AGM demonstrated T2 contrast ability with a high r_2 value (121.77 mM^{-1} s^{-1}) at 7 T field strength, indicating its potential as an excellent T2 contrast agent under ultra-high field strength. Based on these results, AGM possesses both T1 and T2 dual-mode contrast capabilities,

with higher sensitivity than that of Gd-DTPA. This finding holds significant promise for enhancing the accuracy of disease diagnosis and subsequent treatment.

Anti-Inflammatory and Antioxidant in vitro

4T1 cells were used to evaluate the photothermal anticancer effect of MAGM NPs. The CCK-8 experiment revealed that MX, AGM, and MAGM NPs, without laser irradiation, exhibited no significant toxicity to the cells, with over 80% cell viability (Figure 4A). However, both the AGM and MAGM groups exhibited a similar decrease in cell viability following 808 nm laser irradiation at 1 W/cm² for 5 minutes, with IC50 values of 108 μg/mL and 100 μg/mL, respectively. At a concentration of 200 μg/mL, cell viability was reduced to only about 15% for both groups. This demonstrates that the photothermal treatment with AGM and MAGM NPs exerted a significant cytotoxic effect on 4T1 cells. Afterwards, C6@AGM was synthesized to facilitate nanoparticle tracking, and the uptake of nanoparticles by 4T1 cells was assessed using flow cytometry and CLSM (Figure 4B and C). Within the initial 6 hours, the fluorescence intensity in 4T1 cells increased with the incubation time, reaching its peak at 6 hours. Subsequently, the rate of uptake slowed down compared to the rate of metabolism, leading to a reduction in nanoparticle content.

To optimize the photothermal therapy efficacy in cells, we selected a time interval of 6 hours after the addition of AGM and MAGM NPs for laser application in subsequent experiments. To further investigate the photothermal treatment effects of MX, AGM, and MAGM NPs on 4T1 cells, a live and dead cell staining experiment was conducted (Figure 4D). In the absence of NIR irradiation, cells in the MX, AGM, and MAGM groups displayed comparable viable cell densities to the control group, with only a small proportion of cells showing signs of death. This indicates that the three treatments did not induce significant toxicity in the cells. In the AGM and MAGM groups subjected to NIR irradiation (1 W/cm², 5 min), a substantial number of dead cells were observed, consistent with the cell survival rates determined by the CCK8 assay under the same conditions (approximately 50%). These findings further confirm that photothermal therapy (PTT) using MAGM NPs effectively induces tumor cell death.

Inflammation induced by photothermal therapy can promote the release of inflammatory factors from macrophages, potentially increasing the risk of cancer recurrence.[12,37–39] We evaluated the cell viabilities of LPS-activated RAW 264.7 cells treated with MX, AGM, and MAGM NPs using the CCK8 assay (Figure 5A). After incubation, the cell viability remained above 80%, suggesting that MX, AGM, and MAGM NPs did not exhibit significant toxicity towards activated RAW 264.7 cells. Therefore, it was speculated that these treatments did not inhibit the release of inflammatory factors by causing cell death in RAW 264.7 cells. The uptake of C6@AGM by RAW 264.7 cells was assessed using both flow cytometry and CLSM. The fluorescence signal indicated that uptake peaked at 6 hours post-incubation (Figure 5B and C).

As is well known, activated macrophages are often accompanied by oxidative stress.[40–44] Therefore, scavenging excess reactive oxygen species (ROS) provides an effective means to inhibit the release of inflammatory factors from macrophages. In comparison to RAW 264.7 cells before activation, intracellular ROS content increased after activation by LPS, as evidenced by a significant rise in fluorescence signal. The anti-inflammatory effect of MX resulted in a reduction of ROS production, resulting in a decrease in the intracellular fluorescence signal. Notably, cells treated with AGM and MAGM NPs exhibited a more significant decrease in fluorescence signal, indicating their excellent ROS scavenging effect within cells (Figure 5D and Figure S9). Given that MAGM NPs possesses both anti-inflammatory and antioxidant capabilities, cells treated with MAGM NPs exhibited the lowest fluorescent signal. This observation indicates that MAGM NPs effectively reduces oxidative stress in macrophages, thereby further inhibiting the release of inflammatory factors by macrophages.

To further verify the inflammatory response induced by photothermal therapy, we assessed the levels of inflammatory cytokines (TNF-α and IL-6) in the various treatment groups using ELISA assay kits. The results depicted in Figure S10 demonstrated a significant increase in the release of TNF-α and IL-6 in the NIR laser treatment group compared to the control group. Specifically, the photothermal therapy group exhibited an 8-fold increase in TNF-α levels and a 3-fold increase in IL-6 levels. These findings strongly indicated the activation of macrophages and the initiation of an inflammatory response, implying that photothermal therapy stimulates the release of inflammatory factors. However, the AGM+L group displayed a notable reduction in inflammatory factors compared to the GM+L group. This effect can

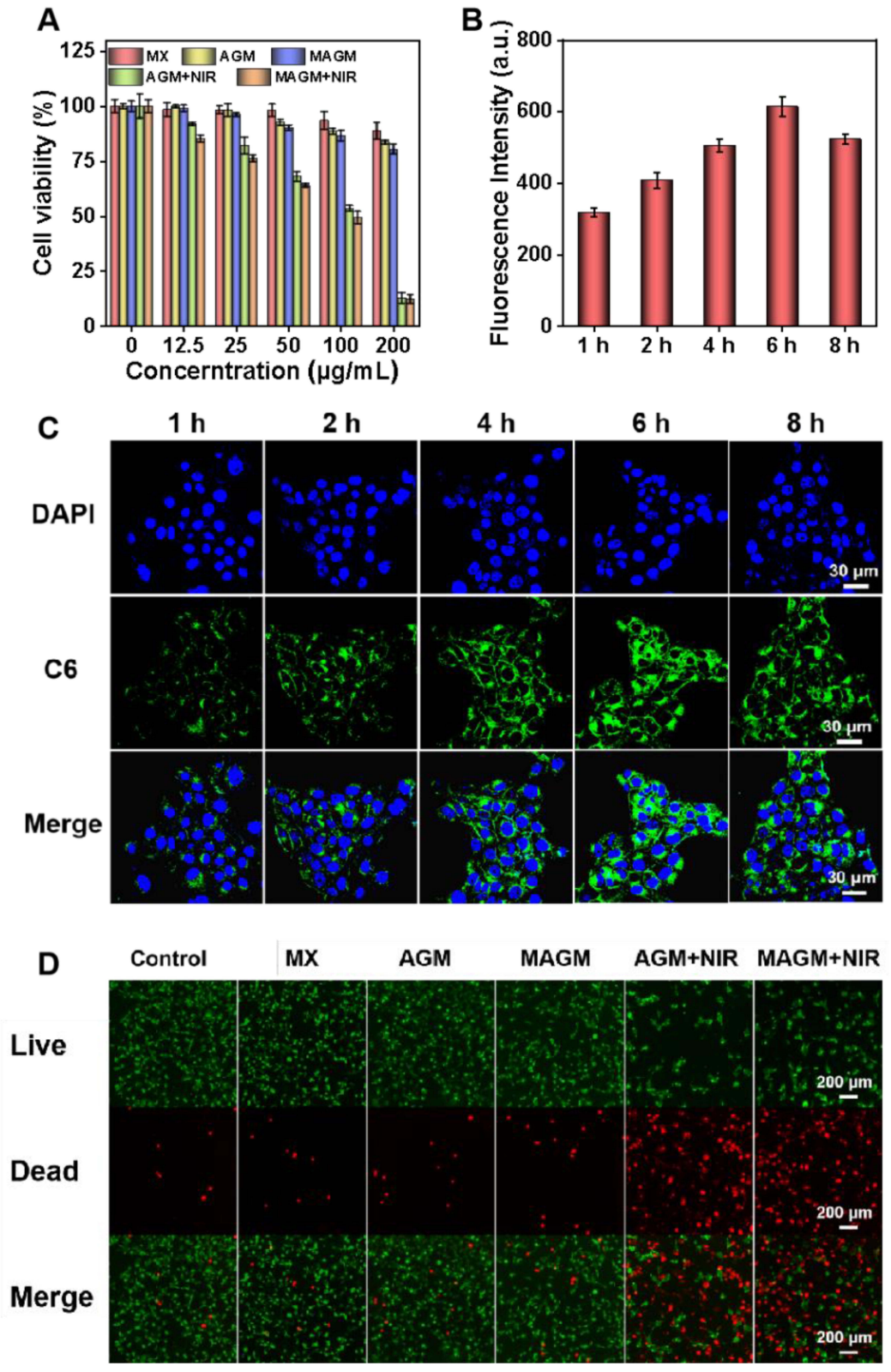

Figure 4 (**A**) Cell viabilities of 4T1 cells after different treatment (NIR: 808 nm, 1 W/cm^2, 3 min); (**B**) fluorescence intensities and (**C**) CLSM images of 4T1 cells after incubation with C6@AGM for different time (Scale bar=30 μm). (**D**) Live and dead cell staining of 4T1 cells after different treatment (L: 808 nm, 1 W/cm2, 3 min) (Scale bar = 200 μm).

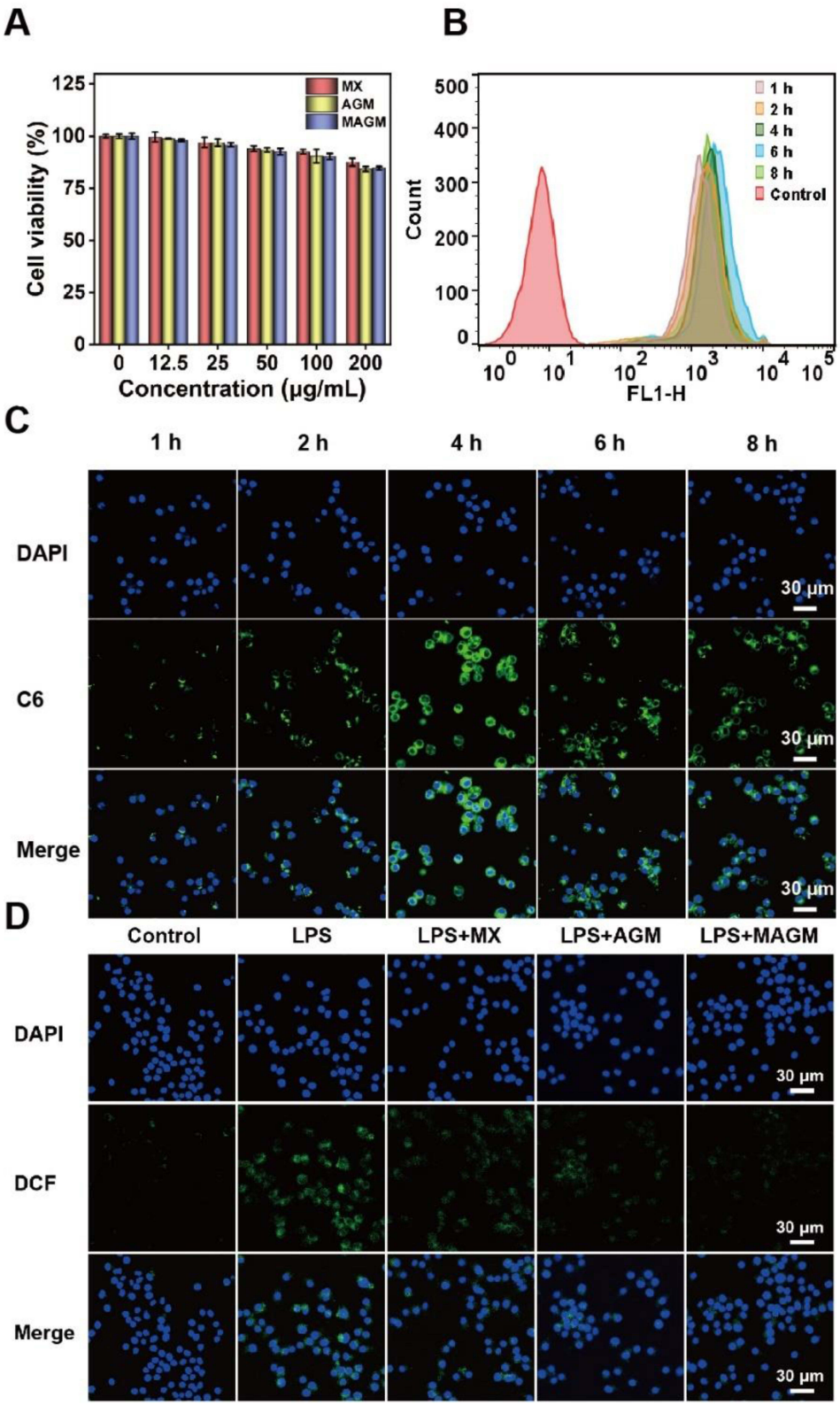

Figure 5 (**A**) Cell viabilities of LPS-activated RAW 264.7 after incubation with different concentrations of MX, AGM and MAGM for 24 h. (**B**) Fluorescence histograms, and (**C**) CLSM images of RAW 264.7 after incubation with C6@AGM for different time. (**D**) CLSM images of LPS-activated RAW 264.7 cells after incubation with MX, AGM and MAGM (Scale bar=30 μm).

be attributed to the inclusion of arginine, which enhanced ROS clearance, thereby inhibiting inflammation. Similarly, the MAGM+L group, incorporating MX-loaded anti-inflammatory drugs, exhibited an amplified antioxidant and anti-inflammatory effect, leading to a more pronounced inhibitory effect on inflammation. These findings contribute to optimizing the therapeutic strategy of photothermal therapy, enhancing its efficacy in cancer treatment.

MRI Imaging and Biodistribution in vivo

In vivo biodistribution analysis of MAGM NPs was conducted on BALB/c mice. As depicted in Figure 6A, the fluorescence signal at the tumor site gradually increased after intravenous injection of Cy5.5@MAGM, peaking at 8 hours, and subsequently decreasing over time. Following 24 hours, the mice were dissected, and the heart, liver, spleen, lungs, kidneys, and tumor were collected to measure the fluorescence signal intensity in various tissues. As depicted in Figure 6B and C, the fluorescence signal of MAGM NPs was predominantly concentrated in the liver, spleen, kidneys, and tumor. This observation indicates that the nanotherapeutic agent is primarily metabolized in the liver, while the fluorescence signal intensity at the tumor site was significantly higher than in other tissues, except for the liver. These findings suggested that MAGM NPs can accumulate at the tumor site, underscoring its potential for cancer diagnosis.

In addition, we assessed the imaging effect of MAGM NPs on tumors by conducting T1 and T2-weighted scans of the tumor site using a 3T MRI at various time points in 4T1 tumor-bearing mice. The T1-weighted signal at the tumor site of mice was weak before the tail vein injection of the nanotherapeutic agent. However, within 0–8 hours after injection, the image contrast at the tumor site gradually increased, reaching its maximum intensity at 8 hours (Figure 6D). As the injection time increased, the signal gradually attenuated, resulting in a progressive darkening of the T1-weighted image,

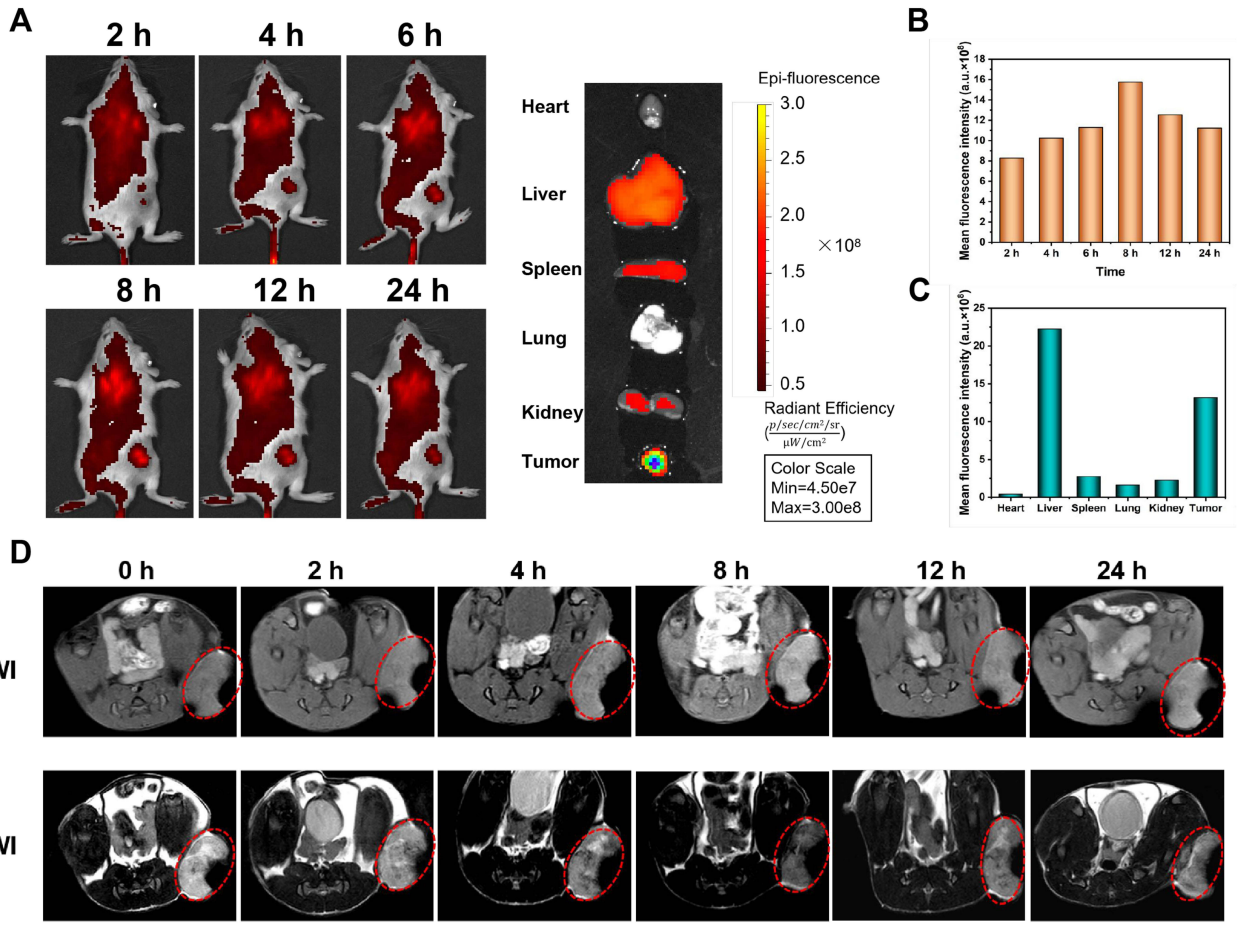

Figure 6 (**A**) The fluorescence imaging and fluorescence intensity were observed at different time points post-injection of MAGM in the tumor site and various organs: (**B**) tumor, (**C**) heart, liver, spleen, lungs, kidneys, and tumor. (**D**) MRI T1 and T2-weighted imaging of the tumor site at different time points.

consistent with the in vivo fluorescence imaging signal. Conversely, in T2-weighted images, the signal at the tumor site in mice gradually increased from 0 to 8 hours, leading to darker images. The strongest signal and the darkest image at the tumor site were observed at 8 hours, followed by signal attenuation and brighter images. These results implied that MAGM NPs enables dual-mode T1/T2 imaging of tumor sites, thereby facilitating cancer diagnosis and guiding cancer treatment.

In vivo Antitumor Efficacy

The therapeutic efficacy of MAGM NPs was evaluated in 4T1 tumor-bearing mice by measuring the changes in tumor size and volume across various treatment groups. Figure 7A demonstrates a notable reduction in tumor size following MAGM NPs photothermal treatment. Furthermore, the tumor volume displayed a suppressed trend at various time points post-treatment. On the 20th day, the tumor volume in the AGM and MAGM groups showed no significant change compared to the PBS group, whereas the AGM+L and MAGM+L groups exhibited a notable decrease (Figure 7B). Specifically, the tumor volume decreased by 2.49-fold in the AGM+L group and by 3.43-fold in the MAGM+L group. These results suggest that AGM displayed notable therapeutic effects on mice under near-infrared light, and the drug-loaded MAGM NPs demonstrated even more prominent efficacy. Finally, tumor suppression was assessed by analyzing dissected tumor tissue sections from different treatment groups using H&E and TUNEL staining. Figure 7C summarized the H&E staining results, indicating that tumor cells in the PBS, MX, AGM, and MAGM groups exhibited uniform infiltration without significant damage. In contrast, the AGM+L and MAGM+L groups showed larger interstitial space and lower cell density. The TUNEL staining results further confirmed the absence of noticeable apoptosis in the cells of the PBS, MX, AGM, and MAGM groups, while evident apoptosis was observed in the tumor cells of the AGM+L and MAGM+L groups. Moreover, the MAGM+L group exhibited a higher number of apoptotic tumor cells compared to the AGM+L group. Based on these observations, it can be inferred that MAGM NPs possesses the capability to effectively suppress tumor growth through photothermal treatment and holds promise as a potential therapeutic approach for cancer treatment.

In order to prove that nanoparticles cause inflammatory reaction after photothermal treatment in tumor sites and visualize the corresponding anti-inflammatory effect of nanoparticles, we took out the tumor tissues of different drug groups after treatment, soaked them in PBS (pH=7.4) and crushed them, and then extracted the tissue supernatant by centrifugation to test the changes of cytokine levels (TNF-α, IL-6). As shown in Figure S11, after the treatment, the results of GM+L group showed significantly higher levels of TNF-α and IL-6 after light exposure, indicating that the inflammatory response induced by photothermal heat could not be ignored. Meanwhile, compared with the GM+L group, the MAGM+L in the combined treatment group showed a significant decrease in the corresponding levels of TNF-α and IL-6 at the tumor site due to the effective delivery of the anti-inflammatory drug MX. Taken together, these results indicate that the treatment group MAGM+L can effectively alleviate the inflammatory reaction produced during photothermal therapy and reduce the possibility of tumor recurrence.

Finally, we assessed the safety of MAGM NPs photothermal treatment by monitoring the body weight changes of mice throughout the treatment period. Following the treatment, we conducted HE staining analysis on tissue sections from the heart, liver, spleen, lungs, and kidneys of mice. Additionally, we collected mouse serum for biochemical analysis to evaluate the in vivo safety of the material. The body weight changes of the mice remained within the acceptable range throughout the treatment period, with no significant abnormalities observed (Figure S12). Additionally, serum biochemical analysis revealed that levels of BUN, ALP, ALT, CR, and AST in the mice were within reasonable ranges (Figure 7E and F). HE staining analysis further demonstrated that MAGM NPs photothermal treatment did not cause significant tissue damage (Figure 7D). These findings collectively suggested that photothermal treatment is safe and feasible under experimental conditions.

Statistical Analysis

Data are presented as mean ± standard deviation (mean ± S.D). Differences between two groups were statistically analyzed by unpaired, two-tailed Student's *t* test, while analysis of variance (ANOVA) with Dunnett post hoc test was used for the comparison of data in more than two groups of variables. The levels of significance were set at $*p < 0.05$,

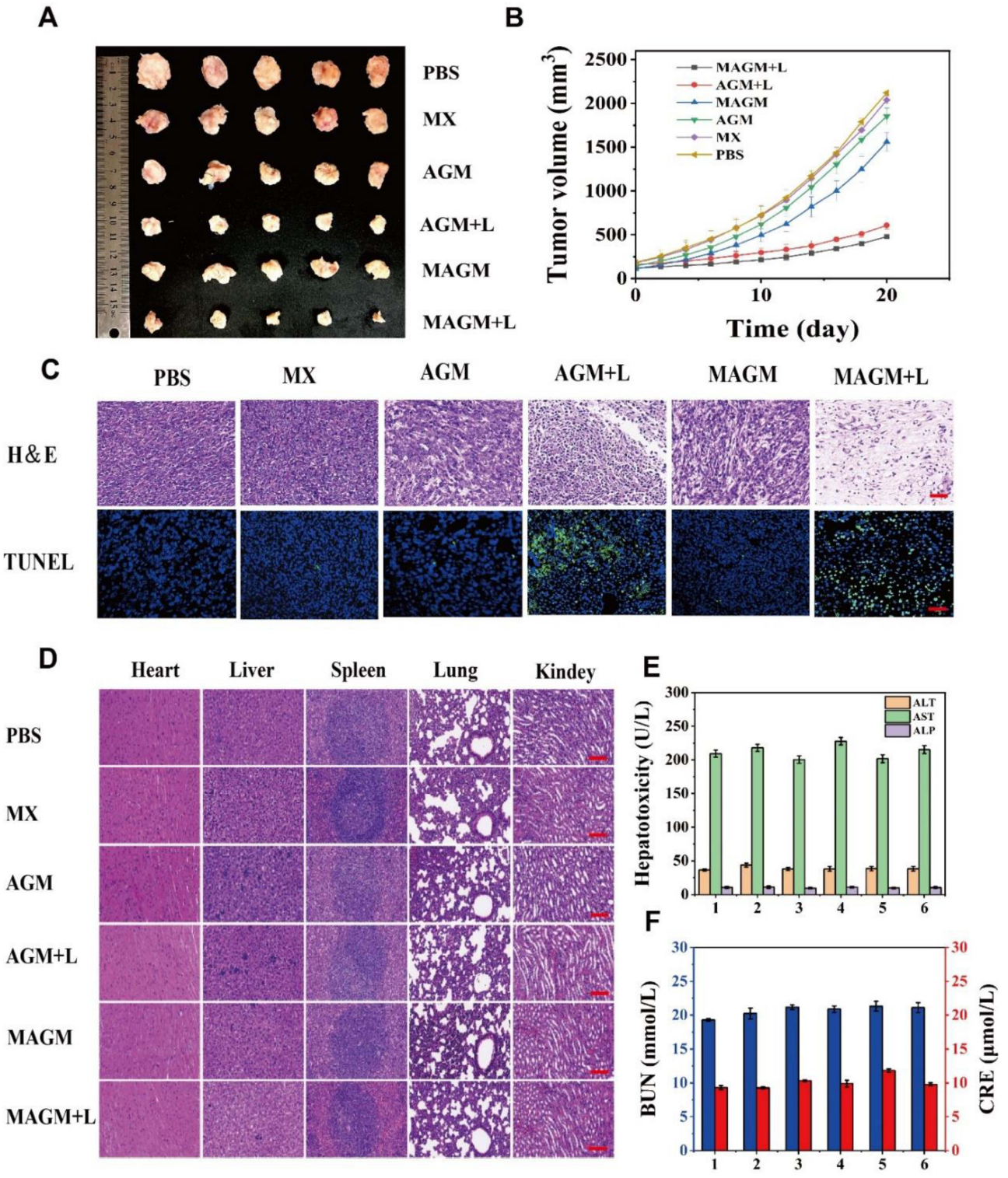

Figure 7 Different treatment groups of 4T1 tumor-bearing mice were evaluated for (**A**) tumor size and (**B**) tumor volume changes as well as histological analysis of tumor sections. (**C**) H&E staining and TUNEL staining of tumor sections (Scale bars= 50 nm). (**D**) H&E staining images of major organs dissected from various groups with different treatments. Scale bars: 50 μm. (**E**) and (**F**) Blood biochemistry tests of the tumor-bearing mice at 20 d after various treatments. 1. PBS; 2. MX, 3. AGM; 4. AGM+L; 5. MAGM; 6. MAGM+L.

**p < 0.01, and ***p < 0.001, respectively. All statistical analyses were performed with GraphPad Prism software version 8 (GraphPad Software, Inc., CA, USA).

Conclusion

An MRI-visible nanotherapeutics MAGM NPs was engineered for MRI-guided photothermal and anti-inflammatory cancer therapy. MAGM NPs exhibited excellent photothermal conversion efficiency for tumor ablation upon localized 808 nm NIR laser irradiation, attributed to Arg doping. Additionally, sustained release of the anti-inflammatory drug MX effectively suppressed the production of inflammatory factors TNF-α and IL-6 at the tumor site, mitigating the inflammatory response induced by PTT. MAGM NPs not only effectively removed ROS from the tumor site, thereby reducing inflammation levels, but also exhibited strong T1-T2 contrast (r_1=74.86 mM^{-1} s^{-1}, r_2=70.66 mM^{-1} s^{-1}) ability due to the chelation of Gd^{3+}. This contrast ability enabled visualization of the retention of MAGM NPs in tumor tissues and guided the combined PTT and anti-inflammatory therapy. Our findings suggested that the development of MAGM NPs represents an effective strategy for multifunctional nanomedicine treatment of breast cancer.

Acknowledgments

This study was supported by the National Natural Science Foundation of China (52073313), Natural Science Foundation of the Guangdong Province (2024A1515010364), Shenzhen Science and Technology Program (2023A002), Science and Technology Program of Guangzhou, China (202002030438) and the Science and the Technology Program of Nansha, China (2023ZD009). In addition, we sincerely thank Wang Kai and Yang Lingjie for their contributions to proofreading manuscripts and MRI imaging, respectively.

Disclosure

The authors declare that they have no competing interests in this work.

References

1. Domingo-Diez J, Souiade L, Manzaneda-González V. et al. Effectiveness of Gold Nanorods of Different Sizes in Photothermal Therapy to Eliminate Melanoma and Glioblastoma Cells. *International Journal of Molecular Sciences*. 2023;24(17):13306. doi:10.3390/ijms241713306
2. Yan X, Li K, Xie T-Q, et al. Bioorthogonal "Click and Release" Reaction-Triggered Aggregation of Gold Nanoparticles Combined with Released Lonidamine for Enhanced Cancer Photothermal Therapy. *Angew Chem Int Ed*. 2024;63(13):e202318539. doi:10.1002/anie.202318539
3. Sadeghi MS, Sangrizeh FH, Jahani N, et al. Graphene oxide nanoarchitectures in cancer therapy: drug and gene delivery, phototherapy, immunotherapy, and vaccine development. *Environ Res*. 2023;237:117027. doi:10.1016/j.envres.2023.117027
4. Chen G, Yang Z, Yu X, et al. Intratumor delivery of amino-modified graphene oxide as a multifunctional photothermal agent for efficient antitumor phototherapy. *J Colloid Interface Sci*. 2023;652:1108–1116. doi:10.1016/j.jcis.2023.08.126
5. Shen K, Yan Y, Xue Z, et al. Multiwalled Carbon Nanotubes Decorated with Mn0.5Zn0.5Fe2O4 Nanoparticles for Magneto-Photothermal Cancer Therapy. *ACS Appl Nano Mater*. 2023;6(14):13330–13341. doi:10.1021/acsanm.3c01929
6. Zhu J, Ouyang N, Zhao R, et al. Black Phosphorus Nanosheets Grafted with Gold Nanorods and Carbon Nanodots for Synergistic Antitumor Therapy. *ACS Appl Mater Interfaces*. 2023;15(22):26241–26251. doi:10.1021/acsami.3c00524
7. Ni C, Lu J, Chen Z, et al. Preparation of polydopamine-based concave nanoparticles and mild photothermal-anti-inflammatory combination therapy for breast cancer guided by magnetic resonance imaging. *Mater Des*. 2023;229:111858. doi:10.1016/j.matdes.2023.111858
8. Tao W, Cheng X, Sun D, et al. Synthesis of multi-branched Au nanocomposites with distinct plasmon resonance in NIR-II window and controlled CRISPR-Cas9 delivery for synergistic gene-photothermal therapy. *Biomaterials*. 2022;287:121621. doi:10.1016/j.biomaterials.2022.121621
9. Tian Y, Younis MR, Tang Y, et al. Dye-loaded mesoporous polydopamine nanoparticles for multimodal tumor theranostics with enhanced immunogenic cell death. *J Nanobiotechnol*. 2021;19(1):365. doi:10.1186/s12951-021-01109-7
10. Diddens-Tschoeke HC, Hüttmann G, Gruber AD, et al. Localized thermal tumor destruction using dye-enhanced photothermal tumor therapy. *Laser Surg Med*. 2015;47(5):452–461. doi:10.1002/lsm.22356
11. Li J, Xie L, Li B, et al. Engineering a Hydrogen-Sulfide-Based Nanomodulator to Normalize Hyperactive Photothermal Immunogenicity for Combination Cancer Therapy. *Adv Mater*. 2021;33(22):2008481. doi:10.1002/adma.202008481
12. Dong Q, Wang X, Hu X, et al. Simultaneous Application of Photothermal Therapy and an Anti-inflammatory Prodrug using Pyrene–Aspirin-Loaded Gold Nanorod Graphitic Nanocapsules. *Angewandte Chemie (International Ed. in English)*. 2018;57(1):177–181. doi:10.1002/anie.201709648
13. Liao T, Chen Z, Kuang Y, et al. Small-size Ti(3)C(2)Tx MXene nanosheets coated with metal-polyphenol nanodots for enhanced cancer photothermal therapy and anti-inflammation. *Acta Biomater*. 2023;159:312–323. doi:10.1016/j.actbio.2023.01.049
14. Zhang L, Zhang Y, Xue Y, et al. Transforming Weakness into Strength: photothermal-Therapy-Induced Inflammation Enhanced Cytopharmaceutical Chemotherapy as a Combination Anticancer Treatment. *Adv Mater*. 2019;31(5):1805936. doi:10.1002/adma.201805936
15. Zhou J, Zhao W, Miao Z, et al. Folin–Ciocalteu Assay Inspired Polyoxometalate Nanoclusters as a Renal Clearable Agent for Non-Inflammatory Photothermal Cancer Therapy. *ACS Nano*. 2020;14(2):2126–2136. doi:10.1021/acsnano.9b08894

16. Lu X, Zhou H, Liang Z, et al. Biodegradable and biocompatible exceedingly small magnetic iron oxide nanoparticles for T(1)-weighted magnetic resonance imaging of tumors. *J Nanobiotechnol*. 2022;20(1):350. doi:10.1186/s12951-022-01562-y
17. Lv S, Sun J, Guo C, et al. PAI/MRI Visualization of Tumor Derived Cellular Microvesicles with Endogenous Biopolymer Nanoparticles Modification. *Int J Nanomed*. 2022;17:2883–2890. doi:10.2147/ijn.S367721
18. Rama E, Mohapatra SR, Melcher C, et al. Monitoring the Remodeling of Biohybrid Tissue-Engineered Vascular Grafts by Multimodal Molecular Imaging. *Adv Sci*. 2022;9(10):e2105783. doi:10.1002/advs.202105783
19. Lin Q, Yang Y, Shao Z. Non-metallic T(2)-MRI agents based on conjugated polymers. *Nat Commun*. 2022;13(1):1994. doi:10.1038/s41467-022-29569-x
20. Jeon M, Halbert MV, Stephen ZR, et al. Iron Oxide Nanoparticles as T1 Contrast Agents for Magnetic Resonance Imaging: fundamentals, Challenges, Applications, and Prospectives. *Adv Mater*. 2021;33(23):1906539. doi:10.1002/adma.201906539
21. Liang M, Zhou W, Zhang H, et al. Tumor microenvironment responsive T(1)-T(2) dual-mode contrast agent Fe(3)O(4)@ZIF-8-Zn-Mn NPs for in vivo magnetic resonance imaging. *J Mater Chem B*. 2023;11(19):4203–4210. doi:10.1039/d3tb00068k
22. Shin T-H, Choi J-S, Yun S, et al. T1 and T2 Dual-Mode MRI Contrast Agent for Enhancing Accuracy by Engineered Nanomaterials. *ACS Nano*. 2014;8(4):3393–3401. doi:10.1021/nn405977t
23. Xiao YD, Paudel R, Liu J, et al. MRI contrast agents: classification and application (Review). *Int J Mol Med*. 2016;38(5):1319–1326. doi:10.3892/ijmm.2016.2744
24. Zhang C, Huang W, Huang C, et al. VHPKQHR Peptide Modified Ultrasmall Paramagnetic Iron Oxide Nanoparticles Targeting Rheumatoid Arthritis for T(1)-Weighted Magnetic Resonance Imaging. *Front Bioeng Biotechnol*. 2022;10:821256. doi:10.3389/fbioe.2022.821256
25. Li H, Hai Z, Zou L, et al. Simultaneous enhancement of T(1) and T(2) magnetic resonance imaging of liver tumor at respective low and high magnetic fields. *Theranostics*. 2022;12(1):410–417. doi:10.7150/thno.67155
26. Huang L, Lu Y, Guo S, et al. A Strategy of Limited-Space Controlled Aggregation for Generic Enhancement of Drug Loading Capability. *Adv Funct Mater*. 2023;33(4):2209278. doi:10.1002/adfm.202209278
27. Dai L, Wei D, Zhang J, et al. Aptamer-conjugated mesoporous polydopamine for docetaxel targeted delivery and synergistic photothermal therapy of prostate cancer. *Cell Proliferation*. 2021;54(11):e13130. doi:10.1111/cpr.13130
28. Wang Y, Ge W, Ma Z, et al. Use of mesoporous polydopamine nanoparticles as a stable drug-release system alleviates inflammation in knee osteoarthritis. *APL Bioeng*. 2022;6(2):026101. doi:10.1063/5.0088447
29. Yang P, Zhang S, Zhang N, et al. Tailoring Synthetic Melanin Nanoparticles for Enhanced Photothermal Therapy. *ACS Appl Mater Interfaces*. 2019;11(45):42671–42679. doi:10.1021/acsami.9b16861
30. Yang P, Gu Z, Zhu F, et al. Structural and Functional Tailoring of Melanin-Like Polydopamine Radical Scavengers. *CCS Chem*. 2020;2(2):128–138. doi:10.31635/ccschem.020.201900077
31. Hou X, Yang X, Xu Y, et al. Manganese-doped mesoporous polydopamine nanoagent for T1–T2 magnetic resonance imaging and tumor therapy. *Nano Res*. 2023;16(2):2991–3003. doi:10.1007/s12274-022-4877-4
32. Liu S, Zhang C, Zhou Y, et al. MRI-visible mesoporous polydopamine nanoparticles with enhanced antioxidant capacity for osteoarthritis therapy. *Biomaterials*. 2023;295:122030. doi:10.1016/j.biomaterials.2023.122030
33. Wang Z, Xie Y, Li Y, et al. Tunable, Metal-Loaded Polydopamine Nanoparticles Analyzed by Magnetometry. *Chem Mater*. 2017;29(19):8195–8201. doi:10.1021/acs.chemmater.7b02262
34. Zandieh M, Liu J. Metal-Doped Polydopamine Nanoparticles for Highly Robust and Efficient DNA Adsorption and Sensing. *Langmuir*. 2021;37(30):8953–8960. doi:10.1021/acs.langmuir.1c00783
35. Hu J, Ding Y, Tao B, et al. Surface modification of titanium substrate via combining photothermal therapy and quorum-sensing-inhibition strategy for improving osseointegration and treating biofilm-associated bacterial infection. *Bioact Mater*. 2022;18:228–241. doi:10.1016/j.bioactmat.2022.03.011
36. Kim YJ, Wu W, Chun SE, et al. Biologically derived melanin electrodes in aqueous sodium-ion energy storage devices. *Proc Natl Acad Sci USA*. 2013;110(52):20912–20917. doi:10.1073/pnas.1314345110
37. Fu Q, Li Z, Ye J, et al. Magnetic targeted near-infrared II PA/MR imaging guided photothermal therapy to trigger cancer immunotherapy. *Theranostics*. 2020;10(11):4997–5010. doi:10.7150/thno.43604
38. Wu W, Pu Y, Gao S, et al. Bacterial Metabolism-Initiated Nanocatalytic Tumor Immunotherapy. *Nano-Micro Lett*. 2022;14(1):220. doi:10.1007/s40820-022-00951-0
39. Zhang D, Yang J, Ye S, et al. Combination of Photothermal Therapy with Anti-Inflammation Therapy Attenuates the Inflammation Tumor Microenvironment and Weakens Immunosuppression for Enhancement Antitumor Treatment. *Small*. 2022;18(13):2107071. doi:10.1002/smll.202107071
40. Muhammad W, Zhu J, Zhai Z, et al. ROS-responsive polymer nanoparticles with enhanced loading of dexamethasone effectively modulate the lung injury microenvironment. *Acta Biomater*. 2022;148:258–270. doi:10.1016/j.actbio.2022.06.024
41. Serfecz JC, Saadin A, Santiago CP, et al. C5a Activates a Pro-Inflammatory Gene Expression Profile in Human Gaucher iPSC-Derived Macrophages. *Int J Mol Sci*. 2021;22(18):18. doi:10.3390/ijms22189912
42. Szeto A, Sun-Suslow N, Mendez AJ, et al. Regulation of the macrophage oxytocin receptor in response to inflammation. *Am J Physiol Endocrinol Metab*. 2017;312(3):E183–e189. doi:10.1152/ajpendo.00346.2016
43. Viaud M, Ivanov S, Vujic N, et al. Lysosomal Cholesterol Hydrolysis Couples Efferocytosis to Anti-Inflammatory Oxysterol Production. *Circ Res*. 2018;122(10):1369–1384. doi:10.1161/circresaha.117.312333
44. Zhao J, Gao W, Cai X, et al. Nanozyme-mediated catalytic nanotherapy for inflammatory bowel disease. *Theranostics*. 2019;9(10):2843–2855. doi:10.7150/thno.33727